The Astrophysical Journal, 754:27 (13pp), 2012 July 20 doi:10.1088/0004-637X/754/1/27

A NEW LOW MAGNETIC FIELD MAGNETAR: THE 2011 OUTBURST OF SWIFT J1822.3−1606

N. Rea[1], G. L. Israel[2], P. Esposito[3], J. A. Pons[4], A. Camero-Arranz[1], R. P. Mignani[5,6], R. Turolla[5,7], S. Zane[5], M. Burgay[3], A. Possenti[3], S. Campana[8], T. Enoto[9], N. Gehrels[10], E. Göğüş[11], D. Götz[12], C. Kouveliotou[13], K. Makishima[14,15], S. Mereghetti[16], S. R. Oates[5], D. M. Palmer[17], R. Perna[18], L. Stella[2], and A. Tiengo[16,19]

[1] Institut de Ciències de l'Espai (CSIC-IEEC), Campus UAB, Facultat de Ciències, Torre C5-parell, E-08193 Barcelona, Spain
[2] INAF–Osservatorio Astronomico di Roma, via Frascati 22, 00040, Monteporzio Catone, Italy
[3] INAF–Osservatorio Astronomico di Cagliari, località Poggio dei Pini, strada 54, I-09012 Capoterra, Italy
[4] Departament de Fisica Aplicada, Universitat d'Alacant, Ap. Correus 99, 03080 Alacant, Spain
[5] Mullard Space Science Laboratory, University College London, Holmbury St. Mary, Dorking, Surrey RH5 6NT, UK
[6] Institute of Astronomy, University of Zielona Góra, Lubuska 2, 65-265, Zielona Góra, Poland
[7] Dipartimento di Fisica e Astronomia, Università di Padova, via F. Marzolo 8, I-35131 Padova, Italy
[8] INAF–Osservatorio Astronomico di Brera, via E. Bianchi 46, I-23807 Merate, Italy
[9] Kavli Institute for Particle Astrophysics & Cosmology (KIPAC), SLAC/Stanford University, P.O. Box 20450, MS 29, Stanford, CA 94309, USA
[10] NASA Goddard Space Flight Center, Greenbelt, MD 20771, USA
[11] Faculty of Engineering and Natural Sciences, Sabancı University, Orhanlı-Tuzla, 34956 İstanbul, Turkey
[12] AIM (CEA/DSM-CNRS-Université Paris Diderot), Irfu/Service d'Astrophysique, Saclay, F-91191 Gif-sur-Yvette, France
[13] NASA Marshall Space Flight Center, Huntsville, AL 35812, USA
[14] High Energy Astrophysics Laboratory, Institute of Physical and Chemical Research (RIKEN), Wako, Saitama 351-0198, Japan
[15] Department of Physics, University of Tokyo, 7-3-1 Hongo, Bunkyo-ku, Tokyo 113-0033, Japan
[16] INAF–IASF Milano, via E. Bassini 15, I-20133 Milano, Italy
[17] Los Alamos National Laboratory, Los Alamos, NM 87545, USA
[18] JILA, University of Colorado, Boulder, CO 80309-0440, USA
[19] IUSS Istituto Universitario di Studi Superiori, viale Lungo Ticino Sforza 56, 27100 Pavia, Italy

Received 2012 March 27; accepted 2012 May 15; published 2012 July 2

ABSTRACT

We report on the long-term X-ray monitoring with *Swift*, *RXTE*, *Suzaku*, *Chandra*, and *XMM-Newton* of the outburst of the newly discovered magnetar Swift J1822.3−1606 (SGR 1822−1606), from the first observations soon after the detection of the short X-ray bursts which led to its discovery, through the first stages of its outburst decay (covering the time span from 2011 July until the end of 2012 April). We also report on archival *ROSAT* observations which detected the source during its likely quiescent state, and on upper limits on Swift J1822.3−1606's radio-pulsed and optical emission during outburst, with the Green Bank Telescope and the Gran Telescopio Canarias, respectively. Our X-ray timing analysis finds the source rotating with a period of $P = 8.43772016(2)$ s and a period derivative $\dot{P} = 8.3(2) \times 10^{-14}$ s s^{-1}, which implies an inferred dipolar surface magnetic field of $B \simeq 2.7 \times 10^{13}$ G at the equator. This measurement makes Swift J1822.3−1606 the second lowest magnetic field magnetar (after SGR 0418+5729). Following the flux and spectral evolution from the beginning of the outburst, we find that the flux decreased by about an order of magnitude, with a subtle softening of the spectrum, both typical of the outburst decay of magnetars. By modeling the secular thermal evolution of Swift J1822.3−1606, we find that the observed timing properties of the source, as well as its quiescent X-ray luminosity, can be reproduced if it was born with a poloidal and crustal toroidal fields of $B_p \sim 1.5 \times 10^{14}$ G and $B_{\rm tor} \sim 7 \times 10^{14}$ G, respectively, and if its current age is ∼550 kyr.

Key words: stars: individual (Swift J1822.3−1606) – stars: magnetars – stars: neutron – X-rays: bursts – X-rays: stars

Online-only material: color figures

1. INTRODUCTION

Sensitive, large field-of-view X-ray monitors, such as the Burst Alert Telescope (BAT) on board *Swift* and the Gamma-ray Burst Monitor on *Fermi*, have proved very useful in magnetar studies. Since the discovery of the first magnetar outbursts (Gavriil et al. 2002; Kouveliotou et al. 2003; Kaspi et al. 2003; Ibrahim et al. 2004), five new members of the class have been discovered through the serendipitous detection of the typical short X-ray bursts emitted by these highly energetic X-ray pulsars, and the accompanying increase in the persistent emission (see Rea & Esposito 2011 for a recent review on magnetar outbursts).

Magnetars, usually recognized in the anomalous X-ray pulsar and soft gamma-ray repeater (SGR) classes, are isolated neutron stars with bright persistent X-ray emission ($L_{\rm X} \sim 10^{33}$–10^{36} erg s^{-1}), rotating at spin periods of ∼0.3–12 s and with large period derivatives (10^{-13} to 10^{-10} s s^{-1}; see Mereghetti 2008; Rea & Esposito 2011 for a review). Sporadically, they emit bursts and flares which can last from a fraction of seconds to minutes, releasing ∼10^{38}–10^{47} erg s^{-1}, and are often accompanied by long-lived (up to years) increases of the persistent X-ray luminosity (outbursts).

The broadband emission of these objects and their flaring activity are believed to be connected to their high dipolar and/or toroidal magnetic field: this is indeed supported by the measurement of surface dipolar B field usually of the order of 10^{14}–10^{15} G (inferred through the assumption that, as ordinary pulsars, they are spun down via magnetic dipolar losses: $B \sim 3.2 \times 10^{19} (P\dot{P})^{1/2}$ G, where P is the spin period in seconds, $\dot{P}$ its first derivative and we assumed a neutron star mass and radius of $R \sim 10^6$ cm and $M \sim 1.4\,M_{\odot}$,

respectively). However, the recent detection of an SGR showing all the typical emission properties defining a magnetar (van der Horst et al. 2010; Esposito et al. 2010), but with an inferred dipolar surface magnetic field $<7.5 \times 10^{12}$ G (Rea et al. 2010), has put into question the need of a high dipolar magnetic field (namely, higher than the quantum electron critical field $B_{\rm Q} = m_e c^2/e\hbar \sim 4.4 \times 10^{13}$ G) for an object to show magnetar-like activity.

On 2011 July 14, a new SGR-like burst and associated outburst were discovered by the *Swift* BAT, and followed soon after by all X-ray satellites (Cummings et al. 2011). The fast slew of the *Swift* X-ray telescope (XRT) promptly detected a new bright X-ray source at R.A.:$18^{\rm h}22^{\rm m}18\overset{\rm s}{.}00$, decl.: $-16^\circ04'26\overset{''}{.}8$ (J2000; $1\overset{''}{.}8$ error at a 90% confidence level; Pagani et al. 2011), with a spin period of $P \sim 8.43$ s (Göğüş & Kouveliotou 2011). The lack of an optical/infrared counterpart (Bandyopadhyay et al. 2011; Rea et al. 2011b; de Ugarte Postigo & Munoz-Darias 2011), as well as the characteristics of the bursts, the X-ray spin period, and its spectral properties (Esposito et al. 2011a, 2011b; Rea et al. 2011a), led to its identification as a new magnetar candidate (Cummings et al. 2011; Halpern 2011).

After the discovery of Swift J1822.3–1606, many attempts were made to measure its spin period derivative (Gogus et al. 2011; Kuiper & Hermsen 2011; Livingstone et al. 2011) in order to estimate its surface dipolar field. We present here the timing and spectral results of the first nine months of X-ray monitoring (Sections 2 and 3) of the new magnetar candidate Swift J1822.3−1606, a detection of its quiescent counterpart in archival data (Section 4), as well as upper limits on its emission in the optical and radio bands (Sections 5 and 6). A detailed study of the SGR-like bursts, accurate X-ray position, and pulse profile modeling will be reported elsewhere (C. Kouveliotou et al. 2012, in preparation). Using our timing and spectral results, we model the source outburst decay, and secular evolution, which resulted in an estimate of the its real age and crustal toroidal field (Section 7).

2. X-RAY OBSERVATIONS AND DATA REDUCTION

In this study, we used data obtained from different satellites (see Figure 1 and Table 1 for a summary). Observations and data analysis are briefly described in the following.

2.1. Swift Data

The XRT (Burrows et al. 2005) on board *Swift* uses a front-illuminated (FI) CCD detector sensitive to photons between 0.2 and 10 keV. Two main readout modes are available: photon counting (PC) and windowed timing (WT). PC mode provides two-dimensional (2D) imaging information and a 2.5073 s time resolution; in WT mode only one-dimensional imaging is preserved, achieving a time resolution of 1.766 ms.

The XRT data were uniformly processed with XRTPIPELINE (version 12, in the HEASOFT software package version 6.11), filtered and screened with standard criteria, correcting for effective area, dead columns, etc. The source counts were extracted within a 20 pixel radius (one XRT pixel corresponds to about $2\overset{''}{.}36$). For the spectroscopy, we used the spectral redistribution matrices in CALDB (20091130; matrices version v013 and v014 for the PC and WT data, respectively), while the ancillary response files were generated with XRTMKARF, and they account for different extraction regions, vignetting, and point-spread function corrections.

Table 1
Swift J1822.3−1606 Observations Used for This Work

Instrument	ObsID	Date[a] (MJD TBD)	Exposure (ks)
Swift/XRT	00032033001 (PC)	55 757.75058	1.6
RXTE/PCA	96048-02-01-00	55 758.48165	6.5
Swift/XRT	00032033002 (WT)	55 758.68430	2.0
Swift/XRT	00032033003 (WT)	55 759.69082	2.0
RXTE/PCA	96048-02-01-05	55 760.80853	1.7
Swift/XRT	00032033005 (WT)	55 761.54065	0.5
RXTE/PCA	96048-02-01-01	55 761.55969	5.0
Swift/XRT	00032033006 (WT)	55 762.24089	1.8
RXTE/PCA	96048-02-01-02	55 762.47384	4.9
Swift/XRT	00032033007 (WT)	55 763.30400	1.6
RXTE/PCA	96048-02-02-00	55 764.61846	6.1
RXTE/PCA	96048-02-02-01	55 765.46687	6.8
Swift/XRT	00032033008 (WT)	55 765.85252	2.2
Swift/XRT	00032033009 (WT)	55 766.28340	1.7
RXTE/PCA	96048-02-02-02	55 767.59064	3.0
RXTE/PCA	96048-02-02-03	55 769.35052	3.4
Swift/XRT	00032033010 (WT)	55 769.49531	2.1
Swift/XRT	00032033011 (WT)	55 770.39936	2.1
Chandra/HRC-I	13511	55 770.83049	11.7
Swift/XRT	00032033012 (WT)	55 771.23302	2.1
RXTE/PCA	96048-02-03-00	55 771.34185	6.8
Swift/XRT	00032033013 (WT)	55 772.40044	2.1
RXTE/PCA	96048-02-03-01	55 774.34999	6.9
RXTE/PCA	96048-02-03-02	55 777.85040	1.9
Swift/XRT	00032051001 (WT)	55 778.10744	1.7
Swift/XRT	00032051002 (WT)	55 779.18571	1.7
RXTE/PCA	96048-02-04-00	55 780.85040	6.7
Swift/XRT	00032051003 (WT)	55 780.49505	2.3
Swift/XRT	00032051004 (WT)	55 781.49878	2.3
RXTE/PCA	96048-02-04-01	55 782.57749	6.2
RXTE/PCA	96048-02-04-02	55 784.97179	6.2
Swift/XRT	00032051005 (WT)	55 786.42055	2.2
Swift/XRT	00032051006 (WT)	55 787.58688	2.2
RXTE/PCA	96048-02-05-00	55 788.05419	6.0
Swift/XRT	00032051007 (WT)	55 788.25617	2.3
Swift/XRT	00032051008 (WT)	55 789.66173	1.7
RXTE/PCA	96048-02-05-01	55 789.95880	6.0
Swift/XRT	00032051009 (WT)	55 790.36270	2.2
RXTE/PCA	96048-02-06-00	55 794.45899	6.5
RXTE/PCA	96048-02-07-00	55 799.61550	6.9
Swift/XRT	00032033015 (WT)	55 800.86278	2.9
Swift/XRT	00032033016 (WT)	55 807.48660	2.4
RXTE/PCA	96048-02-08-00	55 810.37979	6.0
Suzaku/XIS	906002010	55 817.92550	33.5
RXTE/PCA	96048-02-10-00	55 820.23970	6.7
Swift/XRT	00032033017 (WT)	55 822.82836	4.9
Swift/XRT	00032033018 (WT)	55 824.71484	1.5
RXTE/PCA	96048-02-10-01	55826.18540	5.6
XMM-Newton	0672281801	55 827.25350	10.6
Swift/XRT	00032033019 (WT)	55 829.45421	2.3
Swift/XRT	00032033020 (WT)	55 835.54036	2.6
RXTE/PCA	96048-02-11-00	55835.90370	7.0
Swift/XRT	00032033021 (WT)	55 842.06040	4.2
RXTE/PCA	96048-02-12-00	55842.23269	5.8
XMM-Newton	0672282701	55 847.06380	25.8
Swift/XRT	00032033022 (WT)	55 849.61916	3.4
RXTE/PCA	96048-02-13-00	55849.6597976	5.6
Swift/XRT	00032033024 (WT)	55 862.59155	10.2
RXTE/PCA	96048-02-14-00	55863.11100	5.6
Swift/XRT	00032033025 (PC)	55 977.16600	6.3
Swift/XRT	00032033026 (WT)	55 978.53399	10.2
Swift/XRT	00032033027 (PC)	55 981.99499	11.0
Swift/XRT	00032033028 (WT)	55 982.96299	7.0
Swift/XRT	00032033029 (WT)	55 985.17799	7.0

Table 1
(Continued)

Instrument	ObsID	Date[a] (MJD TBD)	Exposure (ks)
Swift/XRT	00032033030 (WT)	55 985.55000	7.0
Swift/XRT	00032033031 (WT)	55 991.09231	6.7
XMM-Newton	0672282901	56022.95692	26.9
Swift/XRT	00032033032 (WT)	56 031.141159	4.3

Note. [a] Mid-point of each observations.

2.2. RXTE Data

The Proportional Counter Array (PCA; Jahoda et al. 1996) on board *RXTE* consists of five collimated xenon/methane multi-anode Proportional Counter Units operating in the 2–60 keV energy range. Raw data were reduced using the FTOOLS package (version 6.11). To study the timing properties of Swift J1822.3−1606, we restricted our analysis to the data in Good Xenon mode, with a time resolution of 1 μs and 256 energy bins. The event-mode data were extracted in the 2–10 keV energy range from all active detectors (in a given observation) and all layers, and binned into light curves of 0.1 s resolution.

2.3. Suzaku Data

Suzaku (Mitsuda et al. 2007) observed the field of Swift J1822.3−1606 on 2012 September 13–14 with the pulsar located at the X-ray Imaging Spectrometer (XIS; Koyama et al. 2007) nominal position. The XIS consists of three FI CCD cameras (XIS0, XIS2, and XIS3), and one that is back-illuminated (XIS1). One of the FI CCDs, XIS2, was not available at the time of our observation. XIS1 and XIS3 were operating in Normal Mode without any option (all the pixels on the CCD are read out every 8 s), while XIS0 was operating with the 1/8 Window option allowing a readout time of 1 s.

For each XIS, 3 × 3 and 5 × 5 edit modes cleaned event data were combined. Following standard practices, we excluded times within 436 s of *Suzaku* passing through the South Atlantic Anomaly and we also excluded the data when the line of sight was elevated above the Earth limb by less than 5°, or less than 20° from the bright-Earth terminator. Moreover, we excluded time windows during which the spacecraft was passing through a cutoff rigidity of below 6 GV. Finally, we removed hot and flickering pixels. The resulting total effective exposure was ∼33.5 ks for each XIS. The SGR net count rates are 0.710(5), 1.180(6), and 1.060(6) count s^{-1} in the XIS0, XIS1, and XIS3, respectively. For the spectral analysis, we used only XIS0 and XIS3, which are the best calibrated cameras, while for the timing analysis we made use only of the XIS0 data, which owing to the 1/8 Window option have a timing resolution adequate to sample the pulsar spin period.

2.4. Chandra Data

The *Chandra X-ray Observatory* has observed Swift J1822.3−1606 with the High Resolution Imaging Camera (HRC-I; Zombeck et al. 1995) on 2011 July 28, for ∼12 ks (ObsID: 13511). Data were analyzed using standard cleaning procedures[20] and CIAO version 4.4. Photons were extracted from a circular region with a radius of 3″ around the source position, including more than 90% of the source photons (see C. Kouveliotou et al. 2012, in preparation for further details on this observation). We inferred an effective HRC-I count rate of 70 ± 1 counts s^{-1}.

2.5. XMM-Newton Data

We observed Swift J1822.3−1606 three times with *XMM-Newton* (Jansen et al. 2001) on 2011 September 23, October 12, and April 5, for ∼10, 25, and 27 ks, respectively. Only the second observation was partially affected by background flares, which were removed during our spectral analysis (see Section 3.1) resulting in a net exposure time of 19.4 ks. Data have been processed using SAS version 11, and we have employed the most updated calibration files available at the time the reduction was performed (2012 April). Standard data screening criteria are applied in the extraction of scientific products. For our analysis we used only the EPIC-pn camera, and we checked that the two MOS cameras gave consistent results. The EPIC-pn camera was set in Prime Large Window mode (timing resolution 48 ms), with the source at the aim point of the camera. We have extracted the source photons from a circular region of 30″ radius, and a similar region was chosen for the background in

[20] http://asc.harvard.edu/ciao/threads/index.html

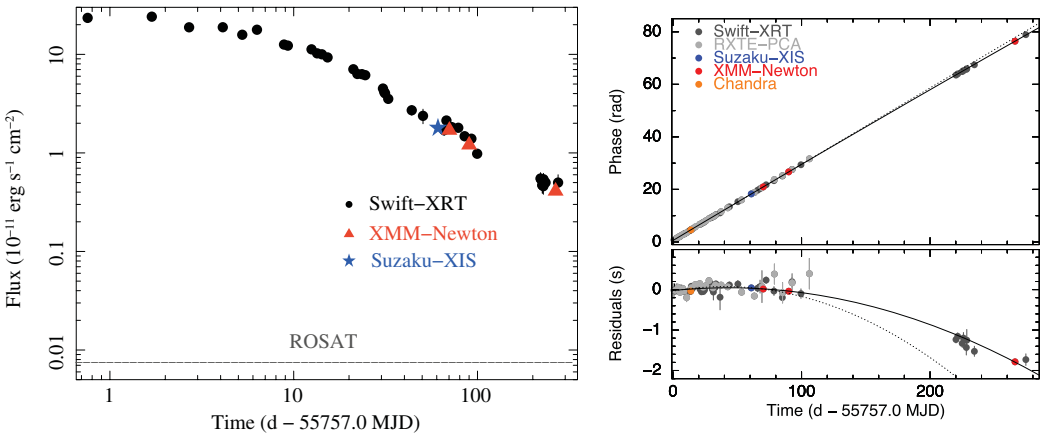

Figure 1. Left panel: flux decay of Swift J1822.3−1606 in the 1–10 keV energy range (see also Table 3). Right panel: pulse phase evolution as a function of time, together with the time residuals (lower panel) after having corrected for the linear component (correction to the P value). The solid lines in the two panels mark the inferred P–$\dot{P}$ coherent solution based on the whole data set, while the dotted lines represent the P–$\dot{P}$ coherent solution based on the data collected during the first 90 days only (see the text for the details).

(A color version of this figure is available in the online journal.)

Table 2
Spectral Analysis of the *Suzaku* and *XMM-Newton* Data

Instrument	Time[a]	Flux[b]	Blackbody + Power Law			Two Blackbodies			
			kT (keV)	R_{BB} (km)[c]	Γ	kT_1 (keV)	R_{BB1} (km)[c]	kT_2 (keV)	R_{BB2} (km)[c]
Suzaku	60.93 ± 0.48	1.78 ± 0.01	0.678 ± 0.008	1.2 ± 0.1	2.90 ± 0.04	0.39 ± 0.01	2.6 ± 0.4	0.79 ± 0.01	0.9 ± 0.1
XMM-Newton	70.25 ± 0.06	1.70 ± 0.01	0.689 ± 0.006	1.1 ± 0.1	2.86 ± 0.03	0.40 ± 0.01	2.6 ± 0.4	0.84 ± 0.01	0.8 ± 0.1
XMM-Newton	90.06 ± 0.11	1.20 ± 0.03	0.679 ± 0.005	1.0 ± 0.1	2.99 ± 0.03	0.37 ± 0.02	2.5 ± 0.4	0.79 ± 0.01	0.7 ± 0.1
XMM-Newton	266.1 ± 0.2	0.4 ± 0.1	0.623 ± 0.008	0.61 ± 0.08	3.05 ± 0.04	0.35 ± 0.01	2.0 ± 0.2	0.78 ± 0.01	0.4 ± 0.1

Notes.
[a] Times are calculated in days from MJD 55 757.0.
[b] Fluxes are in units of 10^{-11} erg s^{-1} cm^{-2}, referred to the BB+PL fit, and calculated in the 1–10 keV energy range. Errors in the table are given at the 1σ confidence level. Reduced χ^2 and absorption values are χ^2_ν/dof =1.05/2522 and $N_{\rm H} = 0.50(1) \times 10^{22}$ cm^{-2}, χ^2_ν/dof =1.06/2522 and $N_{\rm H} = 0.21(1) \times 10^{22}$ cm^{-2}, for the BB+PL and BB+BB models, respectively.
[c] Radii are calculated assuming a distance of 5 kpc.

the same CCD but as far as possible from the source position. We restricted our analysis to photons having PATTERN $\leqslant 4$ and FLAG $= 0$. We find a EPIC-pn (background-subtracted) count rate of 5.03(3), 3.68(2), and 1.42(1) counts s^{-1} for the first, second, and the third observation, respectively.

3. RESULTS OF THE X-RAY MONITORING

3.1. X-Ray Spectral Modeling

Spectra were extracted as explained in Section 2, and rebinned in order to have at least 20 counts per bin in the *Swift* spectra, and 50 counts per bin in the *Suzaku* and *XMM-Newton* spectra. We started our spectral analysis by fitting our higher quality spectra, those from the three *XMM-Newton*/pn and *Suzaku*/XIS03 observations, with several models (using XSPEC version 12.7.0; see Figure 2 and Table 2). Best fits were found using a blackbody plus power-law (BB+PL; χ^2_ν/dof = 1.05/2522) and a two blackbodies (2BBs; χ^2_ν/dof = 1.06/2522) model, all corrected for the photoelectric absorption (`phabs` model with solar abundances assumed from Anders & Grevesse 1989 and photoelectric cross-section from Balucinska-Church & McCammon 1998). The hydrogen column density along the line of sight was fixed to the same value for all of the spectra for a given model. We obtained $N_{\rm H} = 0.50(1)$ and $0.21(1) \times 10^{22}$ cm^{-2} (errors in the text are at 1σ level unless otherwise specified), for the BB+PL and 2BBs model, respectively (see Table 2). In Figure 2, we show the residuals of this spectral modeling, and note that, although statistically the fits can be considered equally good, the BB+BB model departs from the data at higher energies.

Already from this first analysis it is evident how the spectrum is changing in time, although very slowly.

We then expanded our spectral modeling by fitting simultaneously all the *Swift*/XRT, *Suzaku*/XIS03, and *XMM-Newton*/pn spectra. Again both models gave satisfactory fits (see Table 3). The hydrogen column density along the line of sight was fixed to the same values found from the modeling of our previous analysis. Table 3 summarizes the obtained spectral parameters.

For the BB+PL model, we first allowed all parameters to vary freely, and we noticed that the BB temperature was consistent with being constant in time in the early phases of the outburst (most probably changing too little for our spectral analysis to be sensible to its variations). This was visible already from Table 2 when considering only the most detailed spectra. We then tied the BB temperature across all spectra in the first 100 days of the outburst, and we did it similarly for the last spectra (between 200 and 300 days after the trigger). The best fit (reduced χ^2_ν/dof = 1.1/6501) was found with a BB temperature of $kT = 0.660(8)$ keV and $kT = 0.621(7)$ keV, for the early and late times spectra, respectively. More detailed spectra would have certainly disentangled a slow decay between those two values. Figure 3 (left panel) shows the time evolution of the power-law index (Γ) and the BB area. We can see how the latter shrinks as the outburst decays, while the power-law index increases slowly, anti-correlated with the X-ray flux (see also Figure 1, left panel).

On the other hand, for the BB+BB model we noticed that, by leaving all the parameters free to vary across all the spectra, the temperature and the radius of the first blackbody were not varying significantly in time. Similarly to the BB+PL case, we then fixed those values to be the same in all spectra at early and late times separately. This resulted in the best-fit values of $kT_1 = 0.388(8)$ keV and BB Radius$_1 = 2.5(1)$ km, and $kT_1 = 0.358(7)$ keV and BB Radius$_1 = 1.9(1)$ km (to estimate the BB radii we assume a source distance of 5 kpc). The best fit had a reduced χ^2_ν/dof = 1.1/6542. The second blackbody has a relatively steady temperature around ~0.7 keV (see Figure 3, right panel) and its radius shrinks during the outburst decay.

In the late-time spectra, taken >200 days after the outburst onset, the source flux decreases substantially (from ~24 to 0.4×10^{-11} erg s^{-1} cm^{-2}), as the spectrum continues to soften.

We have also tried to model the spectra with a resonant cyclotron scattering model (Rea et al. 2007, 2008; Zane et al. 2009), and, although the fits gave a good χ^2 value ($\chi^2_\nu \sim 1.1/5912$), the low magnetic field of Swift J1822.3−1606 (see Section 3.2) makes the use of those models, envisaged for $B \sim 10^{14}$ G, questionable (see also Turolla et al. 2011).

We note that, although the χ^2 values of both the BB+PL and BB+BB fits might appear not acceptable from a purely statistical point of view, many systematic errors are present in the simultaneous spectral modeling of different satellites (the most severe being the uncertainties in the intercalibration between them, which is believed to be within a 5% error). We did not add any systematic error in the spectral fitting to show the pure residuals of the fit; however, with only 5% systematic error, the reduced χ^2 values would decrease substantially, reaching a fully acceptable fit for both models ($\chi^2_\nu \sim 1.0$).

3.2. X-Ray Timing Analysis

For the X-ray timing analysis, we used all data listed in Table 1, after referring the event arrival times to the barycenter of the solar system (assuming the source coordinates by Pagani et al. 2011 and the DE200 ephemeris for the solar system).

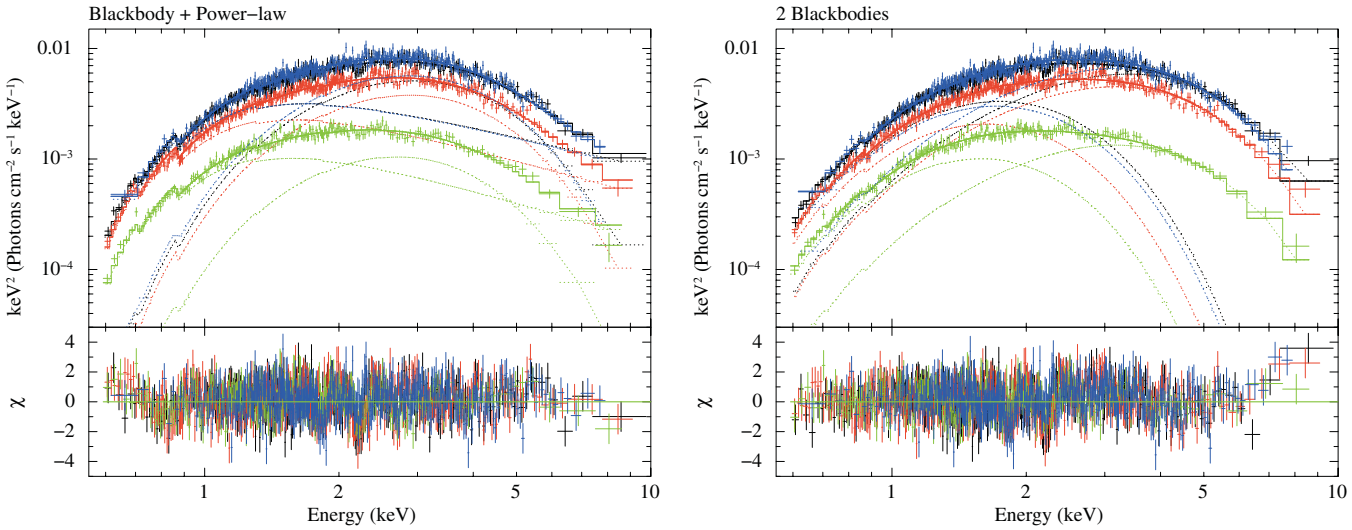

Figure 2. Spectra of the *Suzaku* (blue) and *XMM-Newton* observations fitted together with a blackbody plus power-law and two-blackbody models (see the text and Table 2 for details).

(A color version of this figure is available in the online journal.)

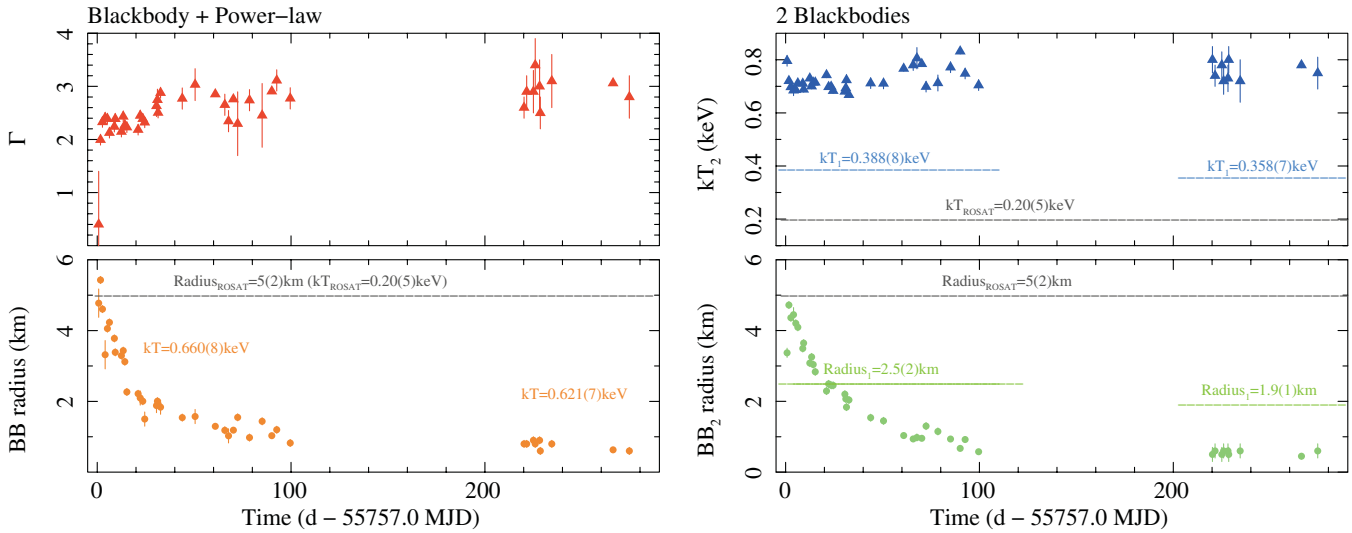

Figure 3. Left panel: spectral parameters for a blackbody plus power-law fit. Right panel: spectral parameters for a two-blackbody fit (see the text and Table 3 for details).

(A color version of this figure is available in the online journal.)

The first *Swift*/XRT event lists were used in order to start building up a phase-coherent timing solution and to infer the SGR timing properties. We started by obtaining an accurate period measurement by folding the data from the first two XRT pointings which were separated by less than one day, and studying the phase evolution within these observations by means of a phase-fitting technique (see Dall'Osso et al. 2003 for details). Due to the possible time variability of the pulse shape we decided not to use a pulse template in the cross-correlation, which might artificially affect the phase shift, and we instead fit each individual folded light curve with two sine functions, the fundamental plus the first harmonic. In the following, we also implicitly assume that the pulsation period (and its derivative) is a reliable estimate of the spin period (and its derivative), an assumption which is usually considered correct for isolated neutron stars.

The resulting best-fit period (reduced $\chi^2 = 1.1$ for 2 degrees of freedom (dof)) is $P = 8.43966(2)$ s (all errors are given at the 1σ confidence level) at the epoch MJD 55757.0. The above period accuracy of 20 μs is enough to phase-connect coherently the later *Swift*, *RXTE*, *Chandra*, *Suzaku*, and *XMM-Newton* pointings. The procedure was repeated by adding, each time, a further observation folded at the above period, and following the phase evolution of the ascending node of the fundamental sine function best fitting the profile of each observation. The relative phases were such that the signal phase evolution could be followed unambiguously for the whole visibility window until 2011 November (see Figure 1). When adding the *RXTE* data set, we also corrected the output phases by a small constant offset (∼0.02), likely due to the different energy ranges and responses.

We modeled the phase evolution with a polynomial function with a linear plus quadratic term, the inclusion of the latter results in a significant improvement of the fit (an *F*-test gives a probability of 7×10^{-6} that the quadratic component inclusion is not required). The corresponding coherent solution (valid until 2011 November) is $P = 8.43772007(9)$ s and period derivative $\dot{P} = 1.1(2) \times 10^{-13}$ s s^{-1} ($\chi^2 = 132$ for 57 dof;

Table 3
Spectral Analysis

ObsID	Time[c]	Flux[d]	Blackbody + Power Law[a]		Two Blackbodies[b]	
			Γ	BB radius (km)[e]	kT_2 (keV)	BB_2 Radius (km)[e]
33001	0.76 ± 0.01	23.4 ± 1.0	0.4 ± 1.0	4.8 ± 0.4	0.80 ± 0.02	3.37 ± 0.13
33002	1.69 ± 0.01	24.1 ± 0.5	2.0 ± 0.1	5.4 ± 0.1	0.72 ± 0.01	4.7 ± 0.1
33003	2.70 ± 0.01	18.8 ± 0.6	2.3 ± 0.1	4.6 ± 0.1	0.70 ± 0.01	4.4 ± 0.1
33005	4.11 ± 0.01	18.8 ± 0.6	2.4 ± 0.1	3.3 ± 0.4	0.68 ± 0.02	4.4 ± 0.2
33006	5.25 ± 0.20	15.8 ± 0.5	2.4 ± 0.1	4.0 ± 0.1	0.69 ± 0.01	4.2 ± 0.1
33007	6.31 ± 0.08	17.8 ± 0.7	2.1 ± 0.1	4.2 ± 0.1	0.71 ± 0.01	4.1 ± 0.1
33008	8.86 ± 0.07	12.5 ± 0.5	2.2 ± 0.1	3.8 ± 0.1	0.71 ± 0.01	3.5 ± 0.1
33009	9.29 ± 0.04	12.2 ± 0.4	2.4 ± 0.1	3.4 ± 0.1	0.69 ± 0.01	3.6 ± 0.1
33010	12.50 ± 0.04	11.2 ± 0.4	2.1 ± 0.1	3.3 ± 0.1	0.73 ± 0.01	3.1 ± 0.1
33011	13.40 ± 0.07	10.2 ± 0.3	2.4 ± 0.1	3.4 ± 0.1	0.70 ± 0.01	3.2 ± 0.1
33012	14.24 ± 0.04	10.0 ± 0.5	2.2 ± 0.2	3.1 ± 0.1	0.71 ± 0.01	3.0 ± 0.1
33013	15.27 ± 0.01	9.3 ± 0.1	2.2 ± 0.1	2.3 ± 0.1	0.71 ± 0.01	2.8 ± 0.1
51001	21.11 ± 0.10	7.0 ± 0.4	2.2 ± 0.1	2.2 ± 0.1	0.74 ± 0.01	2.3 ± 0.1
51002	22.19 ± 0.16	6.3 ± 0.3	2.4 ± 0.1	2.0 ± 0.2	0.70 ± 0.01	2.5 ± 0.1
51003	23.50 ± 0.08	6.3 ± 0.2	2.4 ± 0.1	2.0 ± 0.1	0.70 ± 0.01	2.4 ± 0.1
51004	24.50 ± 0.14	6.1 ± 0.3	2.3 ± 0.1	1.5 ± 0.2	0.68 ± 0.01	2.4 ± 0.1
51006	30.59 ± 0.01	4.5 ± 0.2	2.6 ± 0.2	1.9 ± 0.2	0.68 ± 0.01	2.2 ± 0.1
51007	31.07 ± 0.07	4.1 ± 0.2	2.7 ± 0.2	2.0 ± 0.1	0.69 ± 0.02	2.1 ± 0.1
51008	31.40 ± 0.01	4.0 ± 0.2	2.5 ± 0.1	1.9 ± 0.1	0.72 ± 0.01	1.8 ± 0.1
51009	32.67 ± 0.01	3.5 ± 0.3	2.9 ± 0.1	1.8 ± 0.2	0.67 ± 0.01	2.0 ± 0.1
33015	43.87 ± 0.10	2.7 ± 0.3	2.8 ± 0.2	1.5 ± 0.1	0.71 ± 0.02	1.5 ± 0.1
33016	50.49 ± 0.31	2.4 ± 0.4	3.0 ± 0.3	1.6 ± 0.1	0.71 ± 0.02	1.4 ± 0.1
6002010	60.93 ± 0.48	1.78 ± 0.03	2.85 ± 0.03	1.30 ± 0.01	0.77 ± 0.01	1.03 ± 0.02
33017	65.83 ± 0.13	1.7 ± 0.2	2.6 ± 0.3	1.2 ± 0.1	0.78 ± 0.02	0.94 ± 0.05
33018	67.72 ± 0.20	2.1 ± 0.2	2.3 ± 0.2	1.0 ± 0.1	0.81 ± 0.04	1.0 ± 0.1
81801	70.25 ± 0.06	1.70 ± 0.03	2.76 ± 0.03	1.19 ± 0.01	0.78 ± 0.01	0.96 ± 0.02
33019	72.45 ± 0.35	1.8 ± 0.1	2.3 ± 0.6	1.5 ± 0.1	0.70 ± 0.02	1.3 ± 0.1
33020	78.54 ± 0.46	1.8 ± 0.1	2.7 ± 0.2	1.0 ± 0.1	0.71 ± 0.03	1.1 ± 0.1
33021	85.06 ± 0.38	1.48 ± 0.15	2.4 ± 0.6	1.4 ± 0.1	0.77 ± 0.02	0.94 ± 0.06
82701	90.06 ± 0.11	1.20 ± 0.03	2.91 ± 0.03	1.03 ± 0.01	0.83 ± 0.01	0.67 ± 0.02
33022	92.62 ± 0.38	1.4 ± 0.1	3.1 ± 0.2	1.2 ± 0.1	0.75 ± 0.02	0.92 ± 0.07
33024	99.57 ± 0.37	0.98 ± 0.06	2.8 ± 0.2	0.8 ± 0.1	0.70 ± 0.02	0.57 ± 0.04
33025	220.2 ± 0.8	0.55 ± 0.08	2.6 ± 0.2	0.8 ± 0.1	0.80 ± 0.05	0.5 ± 0.2
33026	221.5 ± 0.4	0.54 ± 0.06	2.9 ± 0.3	0.8 ± 0.1	0.74 ± 0.04	0.6 ± 0.2
33027	225.0 ± 0.1	0.47 ± 0.08	2.9 ± 0.4	0.9 ± 0.1	0.78 ± 0.05	0.5 ± 0.2
33028	226.0 ± 0.1	0.47 ± 0.08	3.4 ± 0.5	0.8 ± 0.1	0.72 ± 0.05	0.6 ± 0.2
33029	228.2 ± 0.1	0.46 ± 0.08	3.0 ± 0.5	0.9 ± 0.1	0.73 ± 0.05	0.6 ± 0.2
33030	228.5 ± 0.2	0.54 ± 0.08	2.5 ± 0.3	0.6 ± 0.1	0.80 ± 0.05	0.5 ± 0.2
33031	234.5 ± 0.4	0.50 ± 0.08	3.1 ± 0.5	0.8 ± 0.1	0.72 ± 0.08	0.6 ± 0.2
82901	266.1 ± 0.2	0.41 ± 0.02	3.06 ± 0.04	0.63 ± 0.02	0.78 ± 0.01	0.45 ± 0.08
33032	274.5 ± 0.4	0.5 ± 0.1	2.8 ± 0.4	0.6 ± 0.1	0.75 ± 0.06	0.6 ± 0.2

Notes.
[a] The absorption value and the blackbody temperature were fixed to be the same for all spectra of the first and second set: $N_{\rm H} = 0.50(1) \times 10^{22}$ cm^{-2}, $kT = 0.660(8)$ keV, and $kT = 0.621(7)$ keV, for the first and second set of spectra, respectively. Reduced χ^2_ν/dof = 1.1/6501.
[b] The absorption value, blackbody temperature, and radius were fixed to be the same for all spectra of the first and second set: $N_{\rm H} = 0.21(1) \times 10^{22}$ cm^{-2}, $kT_1 = 0.388(8)$ keV, and BB_1 Radius = 2.5(1) km, and $kT_1 = 0.358(7)$ keV and BB_1 Radius = 1.9(1) km, for the first and second set of spectra, respectively. Reduced χ^2_ν/dof = 1.1/6542.
[c] Times are calculated in days from MJD 55 757.0.
[d] Fluxes are in units of 10^{-11} erg s^{-1} cm^{-2}, referred to the BB+PL fit, and calculated in the 1–10 keV energy range. Errors in the table are given at the 1σ confidence level.
[e] Radii are calculated assuming a distance of 5 kpc.

at epoch MJD 55757.0). The above solution accuracy allows us to unambiguously extrapolate the phase evolution until the beginning of the next *Swift* visibility window which started in 2012 February.

The final resulting phase-coherent solution (see also Table 4), once the latest 2012 observations are included, returns a best-fit period of $P = 8.43772016(2)$ s and period derivative of $\dot{P} = 8.3(2) \times 10^{-14}$ s s^{-1} at MJD 55757.0 ($\chi^2 = 145$ for 67 dof; preliminary results were reported in Israel et al. 2012). The above best-fit values imply a surface dipolar magnetic field of $B \simeq 2.7 \times 10^{13}$ G (at the equator), a characteristic age of $\tau_{\rm c} = P/2\dot{P} \simeq 1.6$ Myr, and a spin-down power $L_{\rm rot} = 4\pi I \dot{P}/P^3 \simeq 1.7 \times 10^{30}$ erg s^{-1}(assuming a neutron star radius of 10 km and a mass of 1.4 $M_\odot$).

The final solution has a relatively high rms ($\sim$120 ms) resulting in a best-fit-reduced $\chi^2_\nu = 2.1$. The introduction of high-order period derivatives in the fit of the phase evolution does not result in a significant improvement of the fit ($\chi^2 = 135$

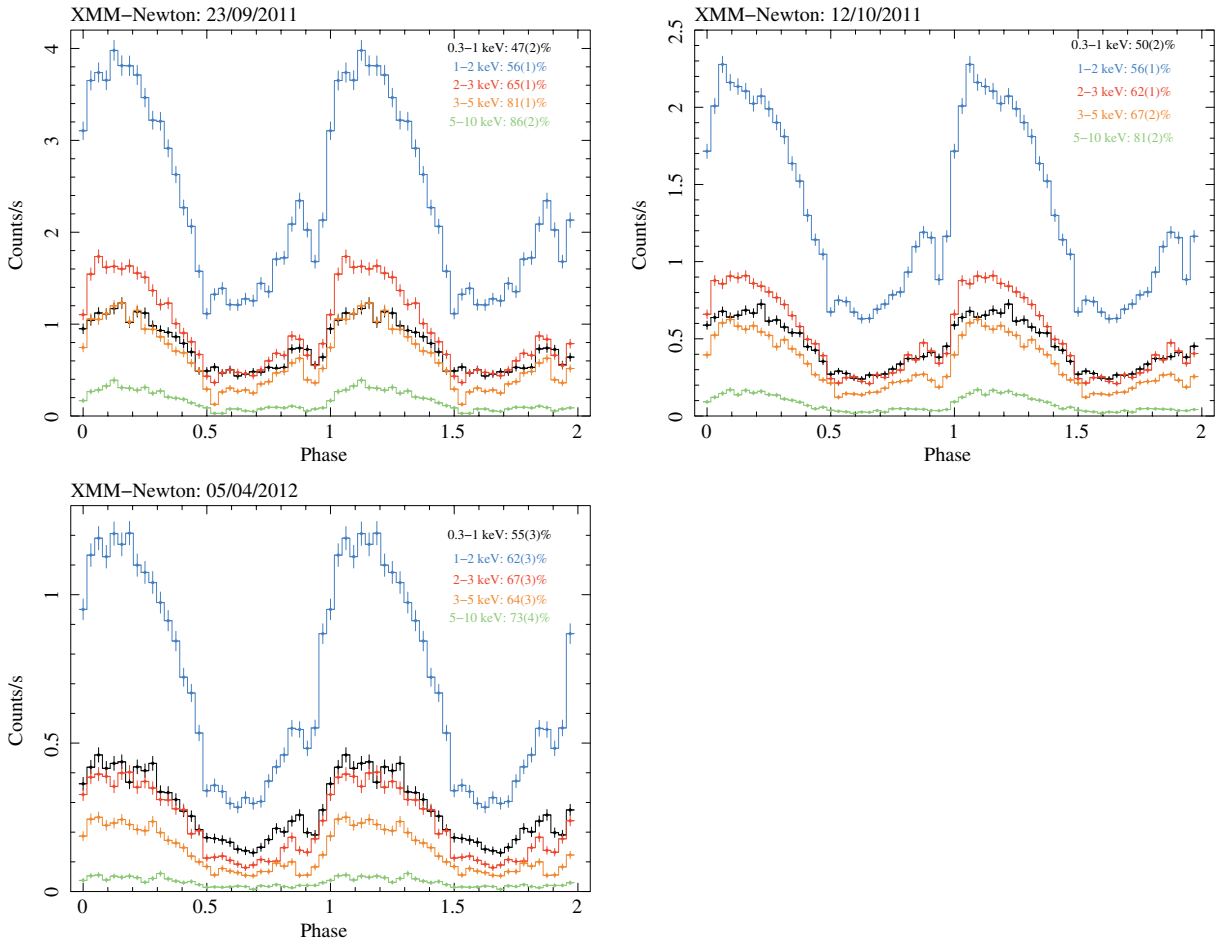

Figure 4. Pulse profiles with 32 bins and relative pulsed fractions as a function of the energy band, for the three *XMM-Newton* observations.
(A color version of this figure is available in the online journal.)

Table 4
Timing Parameters for Swift J1822.3−1606

	Values
Reference epoch (MJD)	55757.0
Validity period (MJD)	55757– 56032
P (s)	8.43772016(2)
$\dot{P}$ (s s^{-1})	$8.3(2) \times 10^{-14}$
$\ddot{P}$ (s s^{-2})	$< 5.8 \times 10^{-21}$
ν (Hz)	0.118515426(3)
$\dot{\nu}$(s^{-2})	$1.17(3) \times 10^{-15}$
$\ddot{\nu}$(Hz s^{-2})	$< 8.1 \times 10^{-23}$
χ^2/dof	145/66
rms residuals (ms)	120
B (Gauss)	2.7×10^{13}
$L_{\rm rot}$ (erg s^{-1})	1.7×10^{30}
$\tau_{\rm c}$ (Myr)	1.6

for 66 dof; an F-test gave a probability of 0.03 that the cubic component inclusion is not required). This results in a 3σ upper limit of the second derivative of the period of $\ddot{P} < 5.8 \times 10^{-21}$ s s^{-2}.

These values of P and $\dot{P}$ are in agreement (within 1σ) with those inferred for the 2011 visibility window reported above.[21] However, this solution is not consistent, within 3σ, with those already reported in the literature and based on a reduced data set (Kuiper & Hermsen 2011; Livingstone et al. 2011; valid until 70 and 90 days from the onset of the outburst, respectively). In order to cross-check our results and to compare them with those previously reported, we fit only those observations of our data set within about 90 days from the trigger. The corresponding best-fit parameters are $P = 8.4377199(1)$ s and period derivative of $\dot{P} = 1.6(4) \times 10^{-13}$ s s^{-1} ($\chi^2 = 119$ for 52 dof; at epoch MJD 55757.0). The latter values are consistent with those of Livingstone et al. (2011).

This analysis, together with the relatively high rms value, suggests that the timing parameters of the pulsar are "noisy." Correspondingly, a timing solution based on a longer baseline may decrease the effect of a noisy behavior, while those reported earlier are likely affected by the shorter timescale variability of the timing parameters.

In Figure 4, we show the pulse profiles as a function of energy for the three *XMM-Newton* observations (see Section 2.5), folded with the best-fit timing solution reported above. We derived pulsed fractions (defined as PF = [Max(counts s^{-1}) − Min(counts s^{-1})]/[Max(counts s^{-1})+ Min(counts s^{-1})]) in the 0.3–1, 1–2, 2–3, 3–5, and 5–10 keV energy bands, of 47% ± 2%, 56% ± 1%, 65% ± 1%, 81% ± 1%, and 86% ± 2%, for the first observation; 50% ± 2%, 56% ± 1%, 62% ± 1%, 67% ± 2%, and 81% ± 2%, for the second observation; and 55% ± 3%, 62% ± 3%, 67% ± 3%, 64% ± 3%, and 73% ± 4%, for the third observation.

[21] Note that the two data sets are not independent. However, we checked that when deriving a timing solution independently using only *RXTE*, *Chandra*, *XMM-Newton*, and *Suzaku* data for the first 120 days, and all the *Swift* observations plus the latest *XMM-Newton* observation for the whole ∼300 days, the two (now independent) solutions are still in agreement within 1σ.

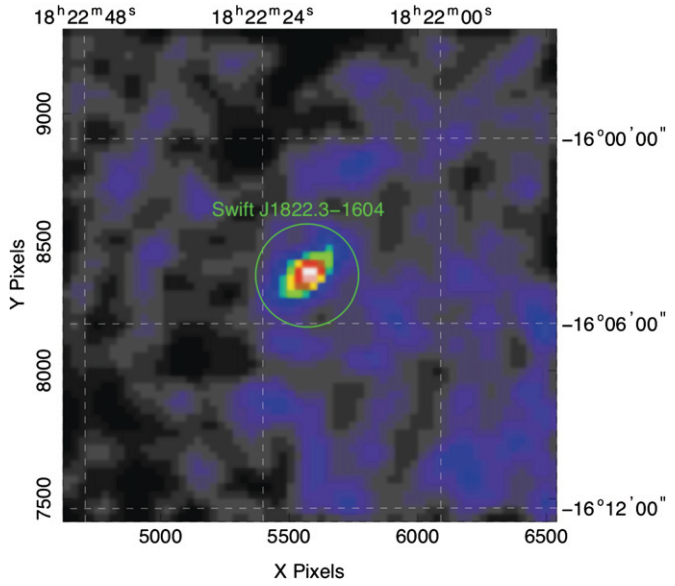

Figure 5. *ROSAT* 1993 image of the region of Swift J1822.3−1606. The circle is centered at the *Swift*/XRT position.

(A color version of this figure is available in the online journal.)

4. *ROSAT* PRE-OUTBURST OBSERVATIONS

The *ROSAT* Position Sensitive Proportional Counter (PSPC; Pfeffermann et al. 1987) serendipitously observed the region of the sky including the position of Swift J1822.3−1606 between 1993 September 12 and 13 (ObsID: rp500311n00), for an effective exposure time of 6.7 ks.

By means of a sliding cell source-detection algorithm, we found a 5.5σ significant source with a 0.1–2.4 keV count rate of 0.012(3) counts s^{-1} at the coordinates R.A. = $18^h22^m18^s.1$, decl. = $-16°04'26''.4$ (positional uncertainty of 30″ radius at the 90% confidence level; J2000). This source is also listed in the WGA (Voges et al. 1999) and RXP (White et al. 1995) catalogs, namely, 1WGA J1822.2–1604 and 2RXP J182217.9–160417, with consistent values of count rate. The positions of the latter objects are ∼20″ and 10″ from the *Swift*/XRT position. Given the relatively large *ROSAT*/PSPC positional uncertainty, we believe the latter two sources and Swift J1822.3−1606 are the same object, which we propose as the SGR quiescent counterpart (see Figure 5).

We downloaded the relevant files of the *ROSAT* pointed observation and extracted the photon arrival times from a circle of ∼100″ radius (corresponding to an encircled energy of >90%) around the X-ray position. We found that an absorbed blackbody with $N_H < 7 \times 10^{21}$ cm^{-2} (see also Section 3.1), $kT = 0.20 \pm 0.05$ keV, and a radius of 5 ± 2 km, best fitted the data (reduced $\chi^2 = 0.8$ for 4 dof). We infer an observed flux of $\approx 1.3 \times 10^{-13}$ erg cm^{-2} s^{-1} and $\approx 4 \times 10^{-14}$ erg cm^{-2} s^{-1} in the 0.1–2.4 keV and 1–10 keV energy ranges, respectively. Assuming a distance of 5 kpc, this flux results in a bolometric luminosity during the quiescence state of $L_{qui} \sim 4 \times 10^{32}$ erg s^{-1}.

No significant periodic signal was found by means of a Fourier transform, even restricting the search around the 8.44 s period. The 3σ upper limits on the pulsed fraction (semi-amplitude of the sinusoid divided by the source average count rate) is larger than 100%.

5. OPTICAL AND INFRARED OBSERVATIONS

We observed the field of Swift J1822.3−1606 with the 10.4 m Gran Telescopio Canarias (GranTeCan) at the Roque de los Muchachos Observatory (La Palma, Spain) (Figure 6). Images were taken in service mode on 2011 July 21 with the OSIRIS camera, a two-chip Marconi CCD detector with a nominal unvignetted 7.′8 × 7.′8 field of view, and an unbinned pixel size of 0.″125. Observations were taken through the Sloan z filter ($\lambda = 969.4$ nm; $\Delta\lambda = 261$ nm). We used a five-point dithering pattern to correct for the effects of the CCD fringing in the red part of the spectrum. We accurately selected the pointing of the telescope to position our target in the right CCD chip and a bright ($B \sim 10$) star ∼54″ east of it in the left one, in order to avoid the contamination from ghost images and saturation spikes. Unfortunately, the observations were taken in conditions of very high sky background due to the high lunar illumination, with the Moon phase at ∼0.5 and angular distance $\lesssim 90°$, and with a seeing ranging from 1″ to 2.″5. Observations were taken using exposure times of 108 and 54 s, with the latter chosen to minimize the sky background induced by the Moon. The total integration time was 4100 s. We reduced the images with the dedicated tools in the IRAF `ccdred` package for bias subtraction and flat-fielding, using the provided bias and sky flat images. We performed the photometric calibration using exposures of the standard star PG 1528+0628. In order to achieve the highest signal to noise, we filtered out observations taken with the highest seeing and sky background. We aligned and co-added all the best images by means of the `swarp` program (Bertin et al. 2002), applying a 3σ filter on the single pixel average to filter out residual hot and cold pixels and cosmic-ray hits. We performed the astrometry calibration of the OSIRIS image with the `WCStools` astrometry package,[22] using as a reference the coordinates of stars selected from the Guide Star Catalog 2 catalog (Lasker et al. 2008). Due to the significant and unmapped CCD distortions, we only obtained an rms of 0.″3 on the astrometric fit. We detected three objects (S1, S2, S3) within or close to the Swift J1822.3−1606 position (see also Rea et al. 2011b; Gorosabel et al. 2011). We computed their flux through standard aperture photometry using the IRAF package `apphot`. Their z-band magnitudes are 18.13 ± 0.16, 20.05 ± 0.04, and 19.94 ± 0.04, for S1, S2, and S3, respectively (see Figure 5). We detected no other object consistent with the refined *Swift*/XRT position of Swift J1822.3−1606 (Pagani et al. 2011) down to a 3σ limiting magnitude of $z = 22.2 \pm 0.2$. Given their bright optical magnitudes, we doubt that any of these objects is the optical counterpart to Swift J1822.3−1606. Based upon GranTecan spectroscopy, de Ugarte Postigo & Munoz-Darias (2011) suggest that S1 and S2 are G- to M-type stars.

As a reference, we inspected images of the Swift J1822.3−1606 field taken prior to our GranTeCan observations, i.e., when Swift J1822.3−1606 was probably in quiescence. To this aim, we searched for near-infrared (IR) observations taken as part of the UK Infrared Deep Sky Survey (UKIDSS; Lawrence et al. 2007), performed with the Wide Field Camera (WFCAM; Casali et al. 2007) at the UK Infrared Telescope (UKIRT) at the Mauna Kea Observatory (Hawaii). The Swift J1822.3−1606 field is indeed included in the UKIDSS Galactic Plane Survey and data are available through Data Release 8 plus. Observations were taken on 2006 May 3 (Bandyopadhyay et al. 2011). We downloaded the fully reduced, calibrated, and co-added J-, H-, K-band science images of the

[22] http://tdc-www.harvard.edu/wcstools/

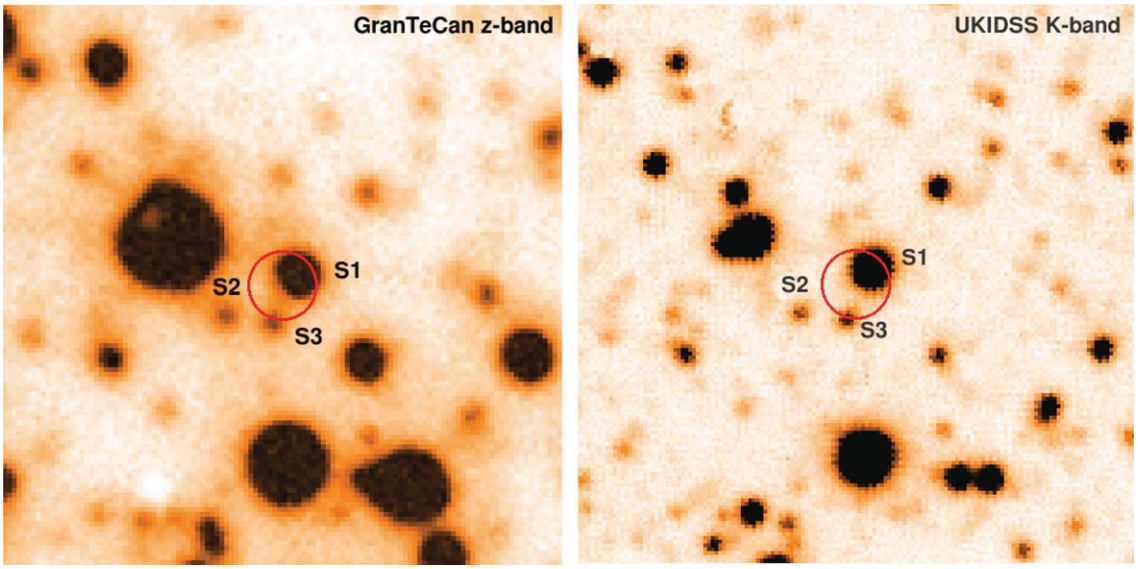

Figure 6. Left panel: GranTeCan image of the Swift J1822.3−1606 field (30″ × 30″) taken with the OSIRIS camera (z band). The circle corresponds to the *Swift*/XRT position of the source (Pagani et al. 2011). The three objects detected close to, or within, the X-ray source error circle are labeled. Right panel: UKIRT image of the same area obtained with the WFCAM in the K band.

(A color version of this figure is available in the online journal.)

Table 5
GBT Radio Observations of Swift J1822.3−1606

Date (YY-MM-DD)	Start Time (MJD)	Exposure (s)	$S_{\rm min}$ (mJy)[a]
11-07-22	55764.268564814818	1031.826964	0.06
11-08-18	55792.008946759262	967.340851	0.06
11-09-20	55824.045960648145	1365.014610	0.05
11-10-19	55853.879884259259	1375.764480	0.05

Note. [a] $S_{\rm min}$ is the minimum flux density reached.

Swift J1822.3−1606 field produced by the UKIDSS pipeline (Hambly et al. 2008) together with the associated object catalogs through the WFCAM Science Archive[23] interface. The WFCAM astrometry is based on the Two Micron All Sky Survey (Skrutskie et al. 2006) and is usually accurate to ∼0.″1 (Lawrence et al. 2007). We clearly identified objects S1 (J = 13.92; H = 12.37; K = 11.62), S2 (J = 16.62; H = 15.75; K = 15.20), S3 (J = 16.43; H = 15.40; K = 14.88) in the UKIDSS images (see Figure 5), with a relative flux comparable to the z-band flux measured on the OSIRIS ones. No other object is detected at the Swift J1822.3−1606 position down to 5σ limiting magnitudes of $J \sim 19.3$, $H \sim 18.3$, and $K \sim 17.3$.

6. RADIO OBSERVATIONS

Radio observations of Swift J1822.3−1606 were performed at the 101 m Green Bank Telescope (GBT) on four occasions after the X-ray outburst, spaced by about a month, one from the other (see Table 5). Data were acquired with the Green Bank Ultimate Pulsar Processing Instrument (DuPlain et al. 2008) at a central frequency of 2.0 GHz over a total observing bandwidth of 800 MHz.

For each observation, in order to correct for the dispersive effects of the interstellar medium, the bandwidth was split into 1024 channels about 250 of which were unusable because of radio frequency interferences (RFI), leaving us with 600 MHz of clean band. The observations lasted 16–23 minutes and were sampled every 0.6557 ms. Since the pulsar rotational parameters are known from X-ray observations (see Section 3.2), we first folded the data at the known period. We also folded the data at half, one-third and a quarter of the nominal period in order to detect putative higher harmonics components of the intrinsic signal, in case the latter were deeply contaminated by RFI. Folding was carried out using DSPSR (van Straten & Bailes 2011) to form 30 s long sub-integrations subdivided into 512 time bins. The sub-integrations and the 1024 frequency channels, cleaned from RFI, were then searched around the nominal period P and over a wide range of dispersion measure (DM) values (from 0 to 1000 pc cm^{-3}) to find the P–DM combination maximizing the signal-to-noise ratio. No dispersed signal was found in the data down to a flux of about 0.05 mJy depending on the observation (see Table 5).

Data were also blindly searched using the code suites PRESTO[24] and SIGPROC.[25] In both cases, after de-dispersion of the data with 839 trial DMs (ranging from 0 to 1000 pc cm^{-3}) and removal of the frequency channels affected by RFI, the time series are transformed using fast Fourier algorithms and their power spectra searched for relevant peaks. These Fourier-based search techniques require a 2^n number of time samples in input; for this reason the amount of data analyzed was 1030 s (a minute of fake data was added to the shortest observation) about two-thirds of the total of the longest observation, hence the flux limit attained, depending on the inverse of the square root of the integration time, was proportionally higher. With SIGPROC we also searched the data for single de-dispersed pulses but no signal was found in either the Fourier domain or the single pulse searches.

[23] http://surveys.roe.ac.uk/wsa/

[24] See http://www.cv.nrao.edu/∼sransom/presto/.

[25] See http://sigproc.sourceforge.net/.

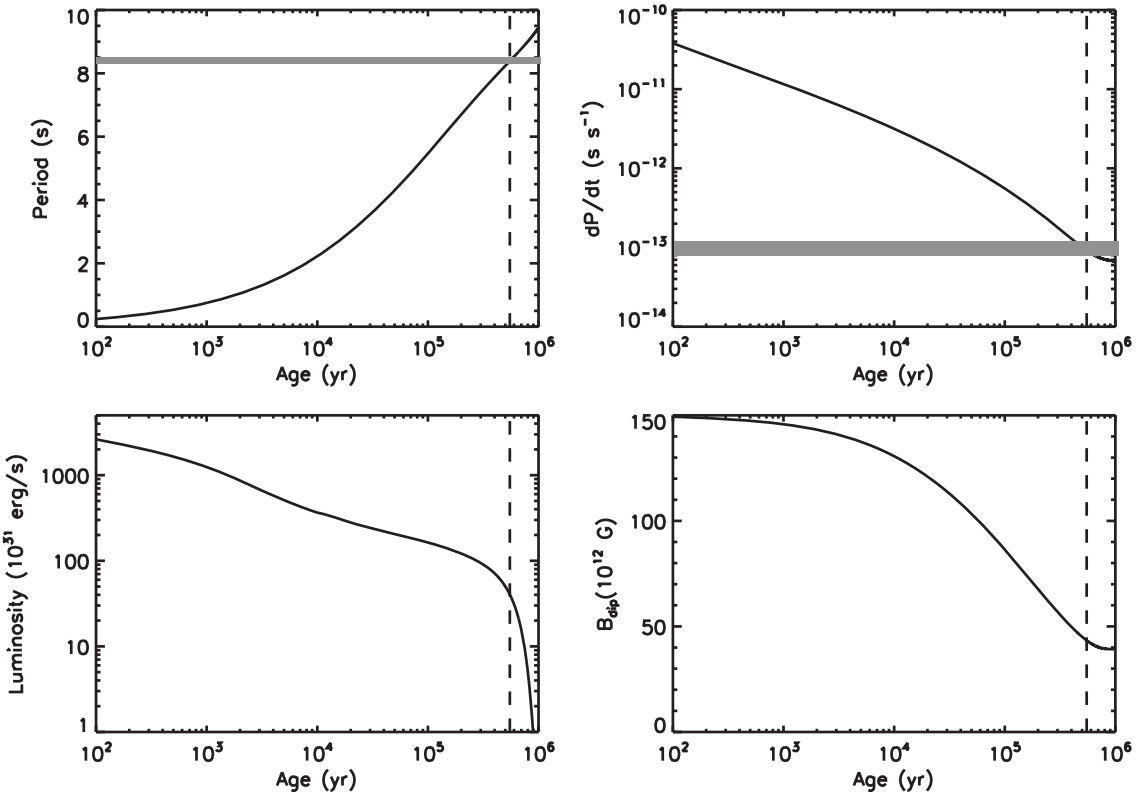

Figure 7. From top left to bottom right, the evolution of the period, period derivative, luminosity, and surface dipole field, according to the model discussed in the text. Gray lines mark the current values of the Swift J1822.3−1606 period and period derivative (with its error). The vertical dashed lines mark the source's "real" age of 550 kyr.

7. DISCUSSION

7.1. The Secular Thermal Evolution of Swift J1822.3−1606

To assess whether the observed properties of Swift J1822.3−1606 are consistent with those of an evolved magnetar, as suggested by its characteristic age of $\tau_c \simeq 1.6$ Myr, we followed the secular evolution of this object using a 2D magneto-thermal evolution code. We refer to Pons et al. (2009) and Aguilera et al. (2008) for details about the code and the microphysical inputs of the model. This allows us to estimate the natal properties of the neutron star, its current age, and internal field strength. We have considered the evolution, including magnetic field decay and heating by Ohmic diffusion, of an ultra-magnetized neutron star with a mass of 1.4 $M_{\odot}$, with no exotic phases nor fast neutrino cooling processes, but with enhanced neutrino emission from the breaking and formation of neutron and proton Cooper pairs (standard cooling scenario). We assumed an initial neutron star spin period of 10 ms and an initial dipolar field of $B_{\rm dip}(t = 0) = 1.5 \times 10^{14}$ G. In Figure 7, we plot the evolution of spin period, period derivative, luminosity, and the dipolar surface magnetic field of a model that can match the current observed values at the "real" age of 550 kyr. The model has an initial crustal toroidal field that reaches a maximum value of $B_{\rm tor-max}(t = 0) = 7 \times 10^{14}$ G (approximately half of the magnetic energy is stored in the toroidal component), which has now decayed to $B_{\rm tor-max} \sim 1.3 \times 10^{14}$ G. We have also studied the expected outburst rate of this source, following the same procedure as in Perna & Pons (2011) and Pons & Perna (2011). We found that at the present stage its outburst rate is very low ($\approx 10^{-3}$ yr^{-1}), because the magnetic field has been largely dissipated.

7.2. The Spectral Evolution During the Outburst

The spectral evolution during the outburst decay in Swift J1822.3−1606 bears resemblance to that observed in other magnetars in outburst, notably XTE J1810−197 (Halpern & Gotthelf 2005; Bernardini et al. 2011), SGR 0501+4516 (Rea et al. 2009), CXOU J1647−4552 (Albano et al. 2010), and the "low field" SGR 0418+5729 (Esposito et al. 2010; Rea et al. 2010; Turolla et al. 2011). In fact the decrease in flux appears to be associated with a progressive spectral softening. Even though present data do not allow for an unambiguous spectral characterization over the entire outburst, evidence for a slow spectral softening is present in both the BB+BB and BB+PL models. In this respect we note that data are not consistent with a BB+PL fit in which the PL index is frozen to the same value in all observations (fitting the values of Γ in Table 3 and Figure 3 with a constant function gives a reduced $\chi^2 > 10$).

A BB+PL spectrum is observed at soft X-ray energies in most magnetar sources, and is interpreted in terms of resonant cyclotron upscattering of thermal surface photons by magnetospheric electrons in a twisted magnetosphere (e.g., Thompson et al. 2002; Nobili et al. 2008). In this framework, the evolution of Swift J1822.3−1606 is compatible with seed photons originating in a relatively small surface region which is heated by the (magnetic) event which gave rise to the outburst, magnetic energy release deep in the crust (as in Lyubarsky 2002), and/or Ohmic dissipation of magnetospheric currents (Beloborodov 2009). The heated region shrinks and cools progressively during the period covered by our observations (the equivalent BB radius decreased from ∼5 km to ∼1 km; in the following we always assume a 5 kpc distance) as residual heat is radiated away and the non-thermal

component shows a progressive softening as the magnetosphere untwists.

On the other hand, the spectral evolution of the source can be also accommodated in the framework of a BB+BB spectral decomposition. In this model, the thermal emission is usually associated with two regions of different temperature and size which were heated during the outburst. It is well possible that a single heated region is actually produced, but with a meridional temperature gradient, which can be schematized as, e.g., a hotter cap surrounded by a warm ring, similarly to the case of XTE J1810−197 (Perna & Gotthelf 2008). The absence of a non-thermal tail is not in contrast with the twisted magnetosphere model if the twist is small and/or it affected only a limited bundle of closed field lines (see, e.g., Esposito et al. 2010), especially if the surface field is low, as in the present source.

The archival *ROSAT* observation shows that, in quiescence, the source has a blackbody spectrum with $kT \sim 0.2$ keV and $R \sim 5$ km. Although the radius is somehow small, it is not unreasonable to associate the *ROSAT* BB with thermal emission from the entire star surface, given the large errors and the uncertain distance determination.

If the outburst produced a heated region, which for concreteness we take to be a two-temperature cap, during the decay we witnessed a gradual shrinking of the hotter region (from ∼5 km to <1 km). The warm ring also shrunk and cooled down slowly during the first 300 days after the outburst. Given the very slow spectral evolution of this component, we could obtain a good spectral modeling by fixing its temperature and radius to be constant during the first 100 days of the outburst, and again (at a different value) in the last 200–300 days (see Figure 3). This should be most probably interpreted as a gradual cooling which could not be followed in detail by the current observations, rather than a temperature jump.

7.3. The Outburst Decay and Timescales

The extensive monitoring campaign we present here allowed us to study in detail the flux decay of Swift J1822.3−1606, and give an estimate of its typical timescale. Fitting the flux evolution in the first 225 days after the onset of the bursting activity, we found that an exponential function or a power law alone cannot fit the data properly, since at later time (50–80 days) the decay slope starts to change. We found an acceptable fit with an analytical function of the form $\mathrm{Flux}(t) = K_1 + K_2 e^{-(t/\tau)} + K_3 t$ ($\chi^2 = 4.7/37$ dof); the best values of the parameters are $K_1 = (1.76 \pm 0.03) \times 10^{-11}$ erg s^{-1} cm^{-2}, $K_2 = (22.0 \pm 0.3) \times 10^{-11}$ erg s^{-1} cm^{-2}, $\tau = 14.6 \pm 0.3$ days, and $K_3 = (-5.2 \pm 0.2) \times 10^{-14}$ erg s^{-1} cm^{-2} day^{-1}. The outburst decays of other magnetars are usually fitted by two components: an initial exponential or power-law component accounting for the very fast decrease in the first days or so (successfully observed only in very few cases), followed by a much flatter power law (see Woods et al. 2004; Israel et al. 2007; Esposito et al. 2008). However, we note that the source has not reached the quiescent level yet; hence the modeling of the outburst, and relative timescale, might change slightly when adding further observations until the truly quiescent level is reached.

We have also compared the observed outburst decay with the more physical theoretical model presented in Pons & Rea (2012). We have performed numerical simulations with a 2D code designed to model the magneto-thermal evolution of neutron stars. The pre-outburst parameters are fixed by fitting the timing properties to the secular thermal evolution presented in Section 7.1. We assume that Swift J1822.3−1606 is presently in an evolutionary state corresponding to that of the model presented in Figure 7 at an age of 550 kyr. We then model the outburst as the sudden release of energy in the crust, which is progressively radiated away. We have run several of such models varying the total injected energy (between 10^{40} and 10^{44} erg), as well as the affected volume, which are the two relevant parameters affecting the outburst decay (coupled with the initial conditions which were explored in Section 7.1). The depth at which the energy is injected and the injection rate bears less influence on the late-time outburst evolution (Pons & Rea 2012).

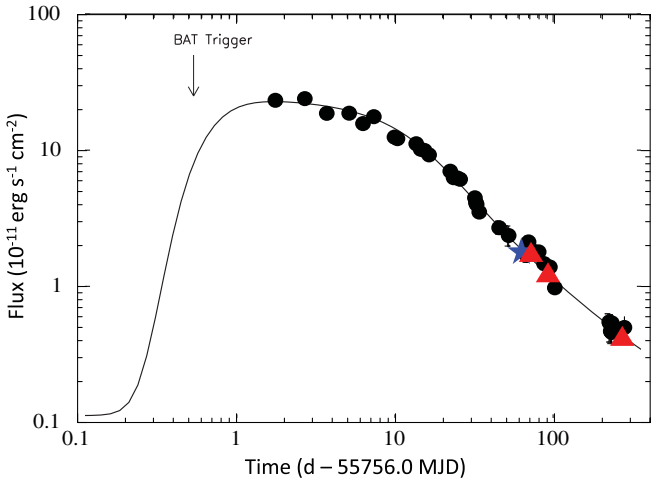

Figure 8. Outburst model from Pons & Rea (2012) superimposed to the 1–10 keV flux decay of Swift J1822.3−1606 (see the text for details).
(A color version of this figure is available in the online journal.)

In Figure 8, we show our best representative model that reproduces the observed properties of the decay of Swift J1822.3−1606 outburst. This model corresponds to an injection of 4×10^{25} erg cm^{-3} in the outer crust, in the narrow layer with density between 6×10^8 and 6×10^{10} g cm^{-3}, and in an angular region of 35 deg (0.6 rad) around the pole. The total injected energy was then 1.3×10^{42} erg.

However, we must note that this solution is not unique and the parameter space is degenerate. Equally acceptable solutions can be found varying the injection energy in the range (1–20) $\times 10^{25}$ erg cm^{-3} and adjusting the other parameters. The outer limit (low density) of the injection region affects the timescale of the rise of the light curve, which is probably too fast (1–10 hr) to be observable in most of the cases. On the other hand, most of the light curve turns out to be insensitive to the inner limit (high density) of the injection region. Only the outburst tail (at >50 days) is affected by this parameter, but this effect is hard to distinguish from similar effects from other microphysical inputs (e.g., varying the impurity content of the crust). Finally, variations of the angular size can be partially compensated by changes in the normalization factor which at present is undetermined (unknown distance). This changes the volume implied and therefore the estimate of the total energy injected. Thus, we need to wait for the full return to quiescence, and combine our study with the complete analysis of the pulse profile and outburst spectrum, before we can place better constraints on the affected volume and energetics.

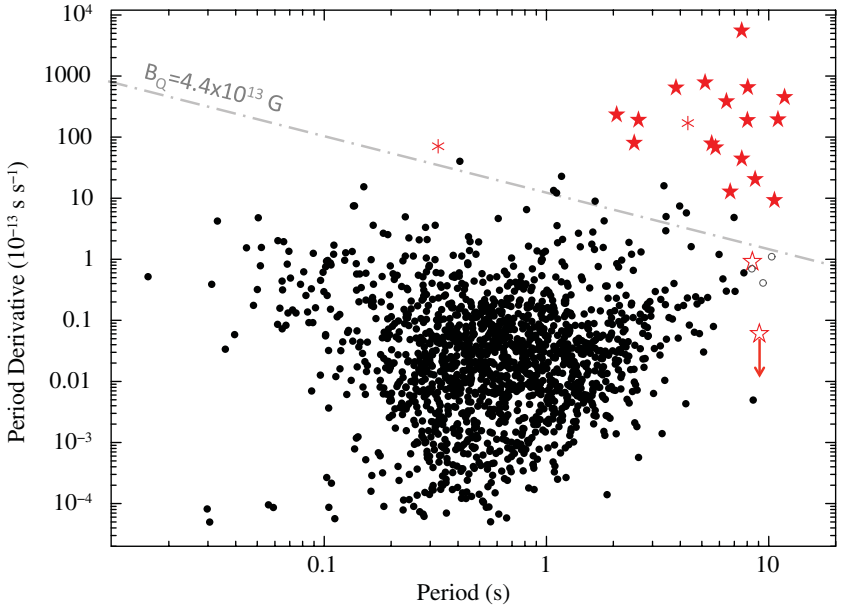

Figure 9. Period–period derivative diagram for all known isolated pulsars. Black dots are radio pulsars (from the ATNF Catalog; Manchester et al. 2005), while red symbols are all known magnetars. Asterisks denote PSR J1846−0258 and PSR 1622−4950, and empty stars are Swift J1822.3−1606 and SGR 0418+5729. Empty gray circles are the X-ray Dim Isolated Neutron Stars (Turolla 2009). The dashed line represents the value of the critical electron magnetic field.
(A color version of this figure is available in the online journal.)

7.4. Radio and Optical Constraints

A recent study on the emission of radio magnetars has shown that all magnetars which exhibited radio-pulsed emission have a ratio of quiescent X-ray luminosity to spin-down power $L_{\rm qui}/L_{\rm rot} < 1$ (Rea et al. 2012). This suggests that the radio activity of magnetars and of radio pulsars might be due to the same basic physical mechanism, while its different observational properties are rather related to the different topology of the external magnetic field (e.g., a dipole and a twisted field; Thompson 2008).

In the case of Swift J1822.3−1606, inferring the quiescent (bolometric) and spin-down luminosities from our *ROSAT* data and our timing results (see Sections 4 and 3.2), we derive $L_{\rm qui}/L_{\rm rot} \simeq 4 \times 10^{32}$ erg s^{-1}/1.7×10^{30} erg s^{-1} $\simeq 235$. This value is in line with the source not showing any radio emission (see Rea et al. 2012 for further details).

Concerning the optical and infrared observations, the bright optical fluxes of the sources S1–S3, much brighter than that of any other SGR in outburst for a comparable distance and interstellar extinction, as well as the lack of relative flux variability, suggest that objects S1–S3 are most likely unrelated to Swift J1822.3−1606. The hydrogen column density derived from the X-ray spectral fits ($N_{\rm H} = 0.5 \times 10^{22}$ cm^{-2}) corresponds to an interstellar extinction $E(B-V) \sim 0.89$ according to the relation of Predehl & Schmitt (1995). Using the wavelength-dependent extinction coefficients of Fitzpatrick (1999), this implies an absorption of $A_z \sim 1.33$ and $A_K \sim 0.32$ in the z and K bands, respectively. Our OSIRIS upper limit would then correspond to an extinction-corrected spectral flux of $\lesssim$16.3 μJy in the z band, or to an integrated flux $\lesssim 1.36 \times 10^{-14}$ erg cm^{-2} s^{-1}. For an assumed Swift J1822.3−1606 distance of 5 kpc, this implies an optical luminosity $L_z \lesssim 4 \times 10^{31}$ erg s^{-1} during the outburst phase. Only very few magnetars are detected in the optical band, the only ones being 4U 0142+614, 1E 1048.1−5937, and SGR 0501+4516, all detected in the I band (see, e.g., Mignani 2011; Dhillon et al. 2011). The optical flux of, e.g., 1E 1048.1−5937 during its recent flaring phase (Wang et al. 2008) corresponds to an I-band luminosity $L_I \sim (4 \pm 2) \times 10^{30}$ erg s^{-1} for an assumed distance of 3 ± 1 kpc (Gaensler et al. 2005). Barring the difference in comparing fluxes obtained through two slightly different filters, our optical luminosity upper limit is about an order of magnitude above the 1E 1048.1−5937 luminosity. Similarly, the flux upper limit derived from the UKIDSS data implies for Swift J1822.3−1606 an IR luminosity $L_K \lesssim 1.1 \times 10^{32}$ erg s^{-1} during the quiescent phase. This upper limit is about an order of magnitude above the computed luminosities of the magnetars' IR counterpart in quiescence and, therefore, it is not very constraining.

8. CONCLUSIONS

We have presented the evolution of the 2011 outburst of the new magnetar Swift J1822.3−1606, which, despite its relatively low magnetic field ($B = 2.7 \times 10^{13}$ G), is in line with the outbursts observed for other magnetars with higher dipolar magnetic fields (similar energetics, flux evolution, and spectral softening during the decay). Furthermore, we showed that the non-detection in the radio band is in line with its high X-ray conversion efficiency ($L_{\rm qui}/L_{\rm rot} \simeq 235$; see also Rea et al. 2012 for further details).

We studied the secular thermal evolution of Swift J1822.3−1606 on the basis of the actual value of its period, period derivative, and quiescent luminosity, and found that the current properties of the source can be reproduced if it has now an age of ∼550 kyr, and it was born with a toroidal crustal field of 7×10^{14} G, which has by now decayed by less than an order of magnitude.

The position of Swift J1822.3−1606 in the P–$\dot{P}$ diagram (see Figure 9) is close to that of the "low" field magnetar SGR 0418+5729 (Rea et al. 2010). Although the fact that both have a sub-critical dipole field is not relevant per se, and the dipolar field in Swift J1822.3−1606 is at least four times higher

than SGR 0418+5729, it is worth stressing that the discovery of a second magnetar-like source with a magnetic field in the radio-pulsar range strengthens the idea that magnetar-like behavior may be much more widespread than what believed in the past, and that it is related to the intensity and topology of the internal and surface toroidal components, rather than only to the surface dipolar field (Rea et al. 2010; Perna & Pons 2011; Turolla et al. 2011).

Monitoring the source until its complete return to quiescence will be crucial to disentangle: (1) its complete spectral evolution during the outburst decay, (2) the possible presence of a second derivative of the rotational period, possibly due to the source timing noise, and (3) further refine the modeling of the outburst and the surface region affected by this eruptive event.

We are indebted to the *Swift*, *RXTE*, *Chandra*, *Suzaku*, and *XMM-Newton* scheduling teams for the extraordinary job in promptly planning all the observations presented in this paper. We acknowledge the extraordinary support of the GTC staff, and in particular Rene Rutten and Carlos Alvarez for the prompt reaction to our ToO trigger. We also thank the GBT staff for scheduling these ToO observations so efficiently. N.R. is supported by a Ramon y Cajal Research Fellowship, and by grants AYA2009-07391, SGR2009-811, TW2010005, and iLINK 2011-0303. The Italian authors are supported by Agenzia Spaziale Italiana (ASI), Ministero dell'Istruzione, Università e Ricerca Scientifica e Tecnologica (MIUR–COFIN), and Istituto Nazionale di Astrofisica (PRIN-INAF) grants. P.E. acknowledges financial support from the Autonomous Region of Sardinia through a research grant under the program PO Sardegna FSE 2007–2013, L.R. 7/2007 "Promoting scientific research and innovation technology in Sardinia." C.K. was partially supported by NASA grant NNH07ZDA001-GLAST.

REFERENCES

Aguilera, D. N., Pons, J. A., & Miralles, J. A. 2008, A&A, 486, 255
Albano, A., Turolla, R., Israel, G. L., et al. 2010, ApJ, 722, 788
Anders, E., & Grevesse, N. 1989, Geochim. Cosmochim. Acta, 53, 197
Balucinska-Church, M., & McCammon, D. 1998, ApJ, 496, 1044
Bandyopadhyay, R. M., Lucas, P. W., & Maccarone, T. 2011, ATel, 3502
Beloborodov, A. M. 2009, ApJ, 703, 1044
Bernardini, F., Perna, R., Gotthelf, E. G., et al. 2011, MNRAS, 418, 638
Bertin, E., Mellier, Y., Radovich, M., et al. 2002, in ASP Conf. Ser. 281, Astronomical Data Analysis Software and Systems XI, ed. D. A. Bohlender, D. Durand, & T. H. Handley (San Francisco, CA: ASP), 228
Burrows, D. N., Hill, J. E., Nousek, J. A., et al. 2005, Space Sci. Rev., 120, 165
Casali, M., Adamson, A., Alves de Oliveira, C., et al. 2007, A&A, 467, 777
Cummings, J. R., Burrows, D., Campana, S., et al. 2011, ATel, 3488
Dall'Osso, S., Israel, G. L., Stella, L., Possenti, A., & Perozzi, E. 2003, ApJ, 599, 485
de Ugarte Postigo, A., & Munoz-Darias, T. 2011, ATel, 3518
Dhillon, V. S., Marsh, T. R., Littlefair, S. P., et al. 2011, MNRAS, 416, L16
DuPlain, R., Ransom, S., Demorest, P., et al. 2008, Proc. SPIE, 7019, 70191D1
Esposito, P., Israel, G. L., Turolla, R., et al. 2010, MNRAS, 405, 1787
Esposito, P., Israel, G. L., Zane, S., et al. 2008, MNRAS, 390, L34
Esposito, P., Rea, N., & Israel, G. L. 2011a, ATel, 3490
Esposito, P., Rea, N., Israel, G. L., & Tiengo, A. 2011b, ATel, 3495
Fitzpatrick, E. L. 1999, PASP, 111, 63
Gaensler, B. M., McClure-Griffiths, N. M., Oey, M. S., et al. 2005, ApJ, 620, L95
Gavriil, F. P., Kaspi, V. M., & Woods, P. M. 2002, Nature, 419, 142
Göğüş, E., & Kouveliotou, C. 2011, ATel, 3542
Gogus, E., Strohmayer, T., & Kouveliotou, C. 2011, ATel, 3503
Gorosabel, J., de Ugarte Postigo, A., Mottola, S., et al. 2011, ATel, 3496
Halpern, J. P. 2011, GCN Circ., 12170
Halpern, J. P., & Gotthelf, E. V. 2005, ApJ, 618, 874
Hambly, N. C., Collins, R. S., Cross, N. J. G., et al. 2008, MNRAS, 384, 637
Ibrahim, A. I., Markwardt, C. B., Swank, J. H., et al. 2004, ApJ, 609, L21
Israel, G. L., Campana, S., Dall'Osso, S., et al. 2007, ApJ, 664, 448
Israel, G. L., Esposito, P., Rea, N., et al. 2012, ATel, 3944
Jahoda, K., Swank, J. H., Giles, A. B., et al. 1996, Proc. SPIE, 2808, 59
Jansen, F., Lumb, D., Altieri, B., et al. 2001, A&A, 365, L1
Kaspi, V. M., Gavriil, F. P., Woods, P. M., et al. 2003, ApJ, 588, L93
Kouveliotou, C., Eichler, D., Woods, P. M., et al. 2003, ApJ, 596, L79
Koyama, K., Tsunemi, H., Dotani, T., et al. 2007, PASJ, 59, 23
Kuiper, L., & Hermsen, W. 2011, ATel, 3665
Lasker, B. M., Lattanzi, M. G., McLean, B. J., et al. 2008, AJ, 136, 735
Lawrence, A., Warren, S. J., Almaini, O., et al. 2007, MNRAS, 379, 1599
Livingstone, M. A., Scholz, P., Kaspi, V. M., Ng, C.-Y., & Gavriil, F. P. 2011, ApJ, 743, L38
Lyubarsky, Y. E. 2002, MNRAS, 332, 199
Manchester, R. N., Hobbs, G. B., Teoh, A., & Hobbs, M. 2005, AJ, 129, 1993
Mereghetti, S. 2008, A&AR, 15, 225
Mignani, R. P. 2011, Adv. Space Res., 47, 1281
Mitsuda, K., Bautz, M., Inoue, H., et al. 2007, PASJ, 59, 1
Nobili, L., Turolla, R., & Zane, S. 2008, MNRAS, 386, 1527
Pagani, C., Beardmore, A. P., & Kennea, J. A. 2011, ATel, 3493
Perna, R., & Gotthelf, E. V. 2008, ApJ, 681, 522
Perna, R., & Pons, J. A. 2011, ApJ, 727, L51
Pfeffermann, E., Briel, U. G., Hippmann, H., et al. 1987, Proc. SPIE, 733, 519
Pons, J. A., Miralles, J. A., & Geppert, U. 2009, A&A, 496, 207
Pons, J. A., & Perna, R. 2011, ApJ, 741, L123
Pons, J. A., & Rea, N. 2012, ApJ, 750, L6
Predehl, P., & Schmitt, J. H. M. M. 1995, A&A, 293, 889
Rea, N., & Esposito, P. 2011, in High-Energy Emission from Pulsars and their Systems, ed. D. F. Torres & N. Rea (Astrophysics and Space Science Proceedings; Berlin: Springer), 247
Rea, N., Esposito, P., Israel, G. L., Tiengo, A., & Zane, S. 2011a, ATel, 3501
Rea, N., Esposito, P., Turolla, R., et al. 2010, Science, 330, 944
Rea, N., Israel, G. L., Turolla, R., et al. 2009, MNRAS, 396, 2419
Rea, N., Mignani, R. P., Israel, G. L., & Esposito, P. 2011b, ATel, 3515
Rea, N., Pons, J. A., Torres, D. F., & Turolla, R. 2012, ApJ, 748, L12
Rea, N., Zane, S., Lyutikov, M., & Turolla, R. 2007, Ap&SS, 308, 505
Rea, N., Zane, S., Turolla, R., Lyutikov, M., & Götz, D. 2008, ApJ, 686, 1245
Skrutskie, M. F., Cutri, R. M., Stiening, R., et al. 2006, AJ, 131, 1163
Thompson, C. 2008, ApJ, 688, 499
Thompson, C., Lyutikov, M., & Kulkarni, S. R. 2002, ApJ, 574, 332
Turolla, R. 2009, in Neutron stars and pulsars, ed. W. Becker (Astrophysics and Space Science Library, Vol. 357; Berlin: Springer), 141
Turolla, R., Zane, S., Pons, J. A., Esposito, P., & Rea, N. 2011, ApJ, 740, 105
van der Horst, A. J., Connaughton, V., Kouveliotou, C., et al. 2010, ApJ, 711, L1
van Straten, W., & Bailes, M. 2011, PASA, 28, 1
Voges, W., Aschenbach, B., Boller, Th., et al. 1999, A&A, 349, 389
Wang, Z., Bassa, C., Kaspi, V. M., Bryant, J. J., & Morrell, N. 2008, ApJ, 679, 1443
White, N. E., Giommi, P., & Angelini, L. 1995, WGA Catalogue of *ROSAT* Point Sources (Greenbelt: NASA/GSFC)
Woods, P. M., Kaspi, V. M., Thompson, C., et al. 2004, ApJ, 605, 378
Zane, S., Rea, N., Turolla, R., & Nobili, L. 2009, MNRAS, 398, 1403
Zombeck, M. V., Chappell, J. H., Kenter, A. T., et al. 1995, Proc. SPIE, 2518, 96